ALMA MATER STUDIORUM
UNIVERSITÀ DI BOLOGNA

ARCHIVIO ISTITUZIONALE
DELLA RICERCA

Alma Mater Studiorum Università di Bologna
Archivio istituzionale della ricerca

First-principles study of structural and surface properties of (001) and (010) surfaces of hydroxylapatite and carbonated hydroxylapatite

This is the final peer-reviewed author's accepted manuscript (postprint) of the following publication:

Published Version:
Ulian, G., Moro, D., Valdre', G. (2016). First-principles study of structural and surface properties of (001) and (010) surfaces of hydroxylapatite and carbonated hydroxylapatite. JOURNAL OF APPLIED CRYSTALLOGRAPHY, 49(6), 1893-1903 [10.1107/S160057671601390X].

Availability:
This version is available at: https://hdl.handle.net/11585/596123 since: 2021-11-29

Published:
DOI: http://doi.org/10.1107/S160057671601390X

Terms of use:

Some rights reserved. The terms and conditions for the reuse of this version of the manuscript are specified in the publishing policy. For all terms of use and more information see the publisher's website.

This item was downloaded from IRIS Università di Bologna (https://cris.unibo.it/).
When citing, please refer to the published version.

(Article begins on next page)

12 October 2024

This is the final peer-reviewed accepted manuscript of

ULIAN, GIANFRANCO; MORO, DANIELE; VALDRE', GIOVANNI: First-principles study of structural and surface properties of (001) and (010) surfaces of hydroxylapatite and carbonated hydroxylapatite. JOURNAL OF APPLIED CRYSTALLOGRAPHY 49. ISSN 0021-8898

DOI: 10.1107/S160057671601390X

The final published version is available online at:
http://dx.doi.org/10.1107/S160057671601390X

Rights / License: The terms and conditions for the reuse of this version of the manuscript are specified in the publishing policy. For all terms of use and more information see the publisher's website.

This item was downloaded from IRIS Università di Bologna (https://cris.unibo.it/)

When citing, please refer to the published version.

First-principles study of structural and surface properties of (001) and (010) surfaces of hydroxylapatite and carbonated hydroxylapatite

Gianfranco Ulian, Daniele Moro and Giovanni Valdrè*

Dipartimento di Scienze Biologiche, Geologiche e Ambientali, Università di Bologna, Piazza di Porta San Donato 1, Bologna, I-40126, Italy. *Correspondence e-mail: giovanni.valdre@unibo.it

Keywords: carbonated hydroxylapatite; surfaces; density functional theory; electrostatic potential; hydroxylapatite.

Since it was first discovered that the main component of the mineral phase of bone, dentine and enamel is made from non-stoichiometric hydroxylapatite [$Ca_{10}(PO_4)_6(OH)_2$; OHAp], many successful efforts have been made to characterize its structure physico-chemically and to use it as a biomaterial for tissue repair and reconstruction. For the latter, it has been suggested that the biomimetic features of OHAp can be improved by vacancies and ionic substitutions, as typically found in natural bone tissues. In the present work, this line of thought has been followed, and the structural and electrostatic potential features of the (001) and (010) surfaces of OHAp and defective type *A*, type *B* and type *AB* carbonated hydroxylapatite (COHAp) have been studied using *ab initio* quantum mechanics at the DFT/B3LYP level. The results are in good agreement with previous experimental and preliminary theoretical work. They provide a deep analysis of the modulation of OHAp features caused by carbonate substitutions, and extend the current knowledge of the structural and surface properties of apatites.

1. Introduction

Among the many biomaterials employed in medical treatment, the calcium apatite minerals have been studied the most because of their similarity to natural mammalian bones (Corno *et al.*, 2010; Dorozhkin, 2009). In fact, the mineral phase of bone tissue is mainly made up of hexagonal hydroxylapatite (OHAp, space group $P6_3/m$, see Fig. 1), but as an Earth crust mineral OHAp occurs as a thermodynamically more stable monoclinic structure (space group $P2_1/b$) (Suda *et al.*, 1995). Apart from its internal symmetry and doubled *b* parameter, the hexagonal polymorph differs in presenting

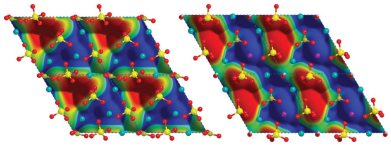

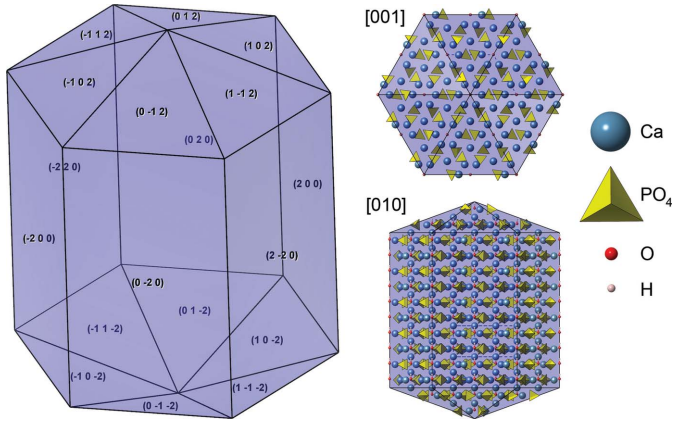

Figure 1
The hydroxylapatite crystal morphology, showing the relevant faces of the mineral and the internal atomic positions.

columns of hydroxyl groups aligned along the *c* axis with O H bonds facing the same direction, while the monoclinic cell exhibits O H columns with alternating orientations (Ma & Liu, 2009).

However, it has also been shown that OHAp is not present in bone tissue in its pure stoichiometric form. Many anionic and cationic substitutions take place in the hydroxylapatite structure, leading to defective hydroxylapatite. Thermodynamically, the presence of substituents and vacancies helps in stabilizing the hexagonal polymorph at room temperature by entropic contributions (Suda *et al.*, 1995). The most common defect is the carbonate anion (CO_3^{2-}), in a weight percentage ranging from 3 to 7%, depending on the function of the tissue and its age (Dorozhkin, 2009). The CO_3^{2-} anion may substitute for both OH^- in the *c*-axis channel of apatite (type *A*) and the PO_4^{3-} group (type *B*). This is confirmed by IR spectra obtained for the two substitutions, where the normal modes of the carbonate group fall at different positions, according to the site occupied by the anion (Fleet, 2009; Fleet & Liu, 2003, 2004). In natural bone tissue, it is common to find both *A* and *B* defects at the same time.

Knowledge of the surface properties of hydroxylapatite, and in particular its defective structures, is of great importance because these features are related to its application as a biomaterial for bone and tooth repair or reconstruction. Some metabolic diseases, such as osteoporosis, hyperparathyroidism and secondary osteolytic tumour effects, cause alterations in the equilibrium of bone neo-deposition and re-absorption (Zhang *et al.*, 2009; Nancollas *et al.*, 2006; Leu *et al.*, 2006; Coxon *et al.*, 2006). Several experimental and theoretical studies have been devoted to the characterization of hydroxylapatite surfaces, both bare and in interaction with different molecules. It is known that the thermodynamic morphology of OHAp is mainly given by the (001) surface (Mkhonto & de Leeuw, 2002; Vallet-Regì & Gonzàlez-Calbet, 2004), but the (010) surface is the most developed in elongated hydroxylapatite platelets during biomineralization and is responsible for the interaction with environmental (biological) molecules (Kirkham *et al.*, 2002; Simmer & Fincham, 1995). As an example, the effect of alendronic acid in interaction with the (001) and (010) OHAp surfaces was studied by the first-principles approach (Canepa *et al.*, 2011), and it was discovered that the pharmacological molecule acts as a protector of the mineral against dissolution.

The physical and chemical design of biomimetic materials for prosthetic purposes must take into account many factors, firstly the compositional and structural atomic/ionic similarities between the biomaterial and the natural tissue, and secondly the fact that the mineral phase is bonded with proteins, mostly tropocollagen, which constitute the organic phase of bone. Thus, characterization of the surface/protein interaction is of great importance, because this knowledge would help in designing resistant biomimetic prosthetic implants. Following these concepts, innovative tensile and compressive stress tests have been conducted by molecular dynamics simulation on two complexes of pure OHAp and tropocollagen fibrils exposed perpendicular to or along the (001) surface of the mineral (Dubey & Tomar, 2009). The interfacial interactions between the mineral and organic phases and structural effects due to the staggered arrangement significantly affect the strength of biomaterials. The simulations also considered the effect of non-hydrated and hydrated environments on the overall OHAp/tropocollagen complex. However, the cited work still represents a 'macroscopic picture' of bone, as the investigation was conducted on mechanical properties on the microscale, and deeper details are still needed to better understand the inorganic/organic matter interface.

A very recent discovery reported the effect induced by the nanoporosity and surface area of hydroxylapatite on stem cell differentiation, which could lead to successful tooth implants (Dangaria *et al.*, 2011). It was shown that natural tooth root topographies induce integrin-mediated extracellular matrix signalling cascades in tandem with cell elongation and polarization to generate physiological periodontium-like tissues. The studies that have been conducted illustrate the capacity of natural extracellular surface topographies to instruct progenitor cell populations to regenerate fully the complex cellular and structural morphologies of tissues once lost to disease.

One possible way of improving the inorganic/organic interaction is to modulate the mineral surface (re)activity by placing a certain proportion of defects in specific locations on the material. The inclusions, substitutions and/or vacancies should be the same as have been found in natural bone, dentine and enamel tissues (Dorozhkin, 2010*a*,*b*, 2009). Also, it was recently found that bone diseases such as osteoporosis establish chemical composition variations on bone apatite, in particular calcium vacancies (Pezzotti *et al.*, 2016). This kind of research has to be conducted on the atomic scale, both for correct placement of the defects and for evaluation of the interaction energies with the target biomolecules. An *ab initio* quantum mechanics (QM) approach, in particular the adoption of density functional theory (DFT), has recently proven to be an excellent choice in the physico-chemical characterization of minerals, at both bulk and surface levels (Ulian *et al.*, 2013*a*,*b*, 2014).

Given the growing interest in the biomineralogical applications of hydroxylapatite and bone disease prevention, in this paper we focus our attention on the (001) and (010) surfaces of OHAp and of carbonated hydroxylapatite (COHAp) to describe their structure reconstruction and activity. We considered every type of carbonate substitution, type *A*, type *B* and mixed type *AB*. Following what has recently been done with DFT/B3LYP/Hay and Wadt pseudopotentials (Hay & Wadt, 1985) by Corno *et al.* (2007), and adopting our recently proposed DFT/B3LYP/all-electron basis set (Ulian *et al.*, 2013*a*,*b*, 2014), we provide structural and surface potential properties of the studied mineral surfaces.

2. Computational details

All the simulations presented in this work were carried out on a Debian (Linux) cluster adopting the periodic *ab initio*

CRYSTAL14 code (Dovesi *et al.*, 2014). With this software it is possible to study periodic systems by the implemented Hartree Fock and Kohn Sham self-consistent field (SCF) method. The molecular graphics program *MOLDRAW* (Ugliengo *et al.*, 1993) was used to obtain and inspect pictures of the structures, while the three-dimensional potential maps were graphically realized with the *VESTA* packge (Momma & Izumi, 2008).

2.1. Basis set

Multi-electron wavefunctions are constructed as an anti-symmetrized product (Slater determinant) of mono-electronic crystalline orbitals that are linear combinations of local functions (atomic orbitals), centred on each atom in the system. In turn, atomic orbitals (basis set) are linear combinations of Gaussian-type functions (GTF). We employed the same all-electron basis sets adopted in our previous work on bulk OHAp and type *A* CAp (Ulian *et al.*, 2013*a*,*b*, 2014). Calcium can be described with an 86-511G(2d) basis, with outer shell exponents α_{sp} = 0.453 bohr^{-2}, α_{d1} = 3.1910 and 0.8683 bohr^{-2} and α_{d2} = 0.2891 bohr^{-2}. The phosphorus atom is described by the basis 85-21G(d), α_{sp} = 0.48105 bohr^{-2} and α_d = 0.135 and 0.74583 bohr^{-2}. Oxygen and hydrogen are both represented by a 6-31G* basis set with the outer shell exponents α_{sp} = 0.2742 and 0.190 bohr^{-2} and α_d = 0.538 bohr^{-2}, and α_{sp} = 0.1613 and α_p = 1.1 bohr^{-2}, respectively. Carbon is described by a 6-21G* basis set with α_{sp} = 0.26 bohr^{-2} and α_d = 0.8 bohr^{-2}.

2.2. Hamiltonian and computational parameters

The Becke (1993) three-parameter (B3LYP) hybrid exchange functional, in combination with the gradient-corrected correlation functional of Lee *et al.* (1988), was adopted for all calculations and has already been widely and successfully used, especially in solid-state calculations (Dovesi *et al.*, 1991; Pascale *et al.*, 2004; Prencipe *et al.*, 2004). The presence of some fraction of exact exchange increases the electronic localization, which in turn increases the ionic nature of the materials, causing a systematic decrease in the lattice parameters and an increase in the elastic constants and bulk moduli. The exchange-correlation contribution is obtained over a grid of points and is the result of numerical integration of the electron density and its gradient. The adopted pruned grid is given by 75 points and 974 angular points (XLGRID) and obtained from the Gauss Legendre quadrature and Lebedev schemes (Prencipe *et al.*, 2004). This is a good compromise between accuracy and cost of calculation for geometry optimization and vibrational frequencies. The tolerance thresholds that control the accuracy of the Coulomb and exchange integrals were set to 10^{-7} and 10^{-14}, respectively (Dovesi *et al.*, 2014). The Hamiltonian matrix was diagonalized using a shrinking factor that leads to 12 and 36 reciprocal lattice points (*k* points) for OHAp and COHAp, respectively. The convergence on total energy was reached when the difference between the energies of two subsequent SCF cycles was less than 10^{-8} hartree.

2.3. Geometry optimization

Full relaxation of the (carbonated) hydroxylapatite surface models (lattice constants and internal coordinates) was performed within the same run, using the analytical gradient method to optimize the atomic positions and a numerical gradient for the cell optimization. The Hessian is updated with the BFGS algorithm. The convergence on surface geometry was controlled by the maximum force, the root mean square (r.m.s.) of the force, the maximum atomic displacement and the r.m.s. atomic displacement, whose thresholds were set to 4.5×10^{-4} hartree bohr^{-1}, 3×10^{-4} hartree bohr^{-1}, 1.8×10^{-3} bohr and 1.2×10^{-3} bohr, respectively. The optimization process ended when each condition was satisfied.

3. Results and discussion

3.1. Hydroxylapatite (001) and (010) surface models and properties

The experimentally refined hexagonal hydroxylapatite has $P6_3/m$ symmetry and it contains two formula units of $Ca_5(PO_4)_3(OH)$ (Z = 2), to give a total of 44 atoms in its unit cell (Hughes *et al.*, 1989). For physical reasons reported elsewhere (Ulian *et al.*, 2013*a*), the computational modelling of this mineral required a lowering of its symmetry to $P6_3$ and, as a consequence, the number of non-equivalent calcium atoms passes from two to three (denoted Ca1, Ca2 and Ca3). The modelling of the OHAp (001) surface follows that proposed earlier by Corno *et al.* (2007), and involves cutting a slab parallel to the (001) plane from the optimized hydroxylapatite bulk geometry. In the present work, the recent OHAp bulk structure obtained with the all-electron basis set was employed (Ulian *et al.*, 2013*a*). The slab thickness is defined by a z range, which limits the number of atoms considered along this direction. This procedure leads to a thin film of the desired thickness, bound by two planes that may also be equivalent by symmetry. The (001) OHAp surface has its symmetry reduced from the bulk $P6_3$ to $P3$, whereas the space group of the (010) OHAp surface was found to be $P2_111$. The solution of the electronic problem using a localized Gaussian basis set allows *CRYSTAL14* to define a real two-dimensional system, without any non-physical replica of the slab along the z coordinate, a common issue that arises when using a plane-wave basis set. Thus, the wavefunction decays to zero at large distances from the upper and lower faces of the defined slab (Dovesi *et al.*, 2014).

In the work of Corno *et al.* (2007), two (001) OHAp slabs of thickness 7 Å (monolayer, ML) and 14 Å (bilayer, BL) were considered. A similar approach was adopted by the authors in their study of water adsorption on the (010) hydroxylapatite surface, where a bilayer slab (13.0 Å thick) was employed (Corno *et al.*, 2009). Despite the authors' statement that a BL slab is adequate for both (001) and (010) surface descriptions, the size of such structures is not sufficient for the aims of the present paper, *i.e.* studying the effects of several CO_3^{2-} substitutions on the thin film properties. For this reason, trilayer (TL) slabs of both the (001) and (010) surfaces were

Table 1
DFT/B3LYP simulation data (present work) compared with X ray diffraction (XRD) single crystal data (Hughes *et al.*, 1989).

Tabulated are the lattice parameters, slab thickness, bulk unit-cell volume V, unit surface area A and selected mean distances of the OHAp bulk and the mono-, bi- and trilayer models of (001) hydroxylapatite. The standard deviations are reported in parentheses. The computed surface energies E_{surf} and band gaps of the three slab models are also reported.

	a (Å)	b (Å)	Thickness (Å)	V (Å^3) or A (Å^2)	⟨P O⟩ (Å)	⟨O H⟩ (Å)	⟨Ca O⟩ (Å)	E_{surf} (J m ^{2})	Band gap (eV)
Bulk	9.433	9.433	6.896	532	1.551	0.971	2.453		7.6
XRD†	9.425	9.425	6.875	528	1.532	1.090	2.460		
(001) surface									
Monolayer	9.252 (3)	9.252 (3)	6.242 (2)	74.126 (4)	1.554 (22)	0.965 (1)	2.41 (10)	1.042	7.9
Bilayer	9.278 (3)	9.278 (3)	13.105 (5)	74.551 (4)	1.555 (15)	0.971 (4)	2.43 (9)	1.146	7.6
Trilayer	9.330 (3)	9.330 (3)	19.945 (7)	75.393 (4)	1.554 (12)	0.972 (4)	2.42 (8)	1.147	7.4
(010) surface									
Monolayer	7.020 (2)	9.187 (3)	9.488 (2)	64.492 (4)	1.558 (40)	0.970 (1)	2.41 (9)	1.390	7.6
Bilayer	6.942 (2)	9.311 (3)	17.580 (4)	64.643 (4)	1.554 (28)	0.971 (1)	2.42 (9)	1.431	7.5
Trilayer	6.927 (2)	9.351 (3)	25.729 (6)	64.773 (4)	1.553 (22)	0.971 (1)	2.48 (8)	1.432	7.5

† X-ray diffraction data from Hughes *et al.* (1989) for comparison.

considered, exhibiting thicknesses of about 19 and 21 Å, respectively (see Figs. 2 and 3). As a complete all-electron basis set for all the atoms was adopted, low-thickness slabs were also modelled to check the convergence of the surface formation energy. The monolayer structure has 44 atoms, as in the unit cell of the bulk ($Z = 2$), the bilayer has 88 atoms ($Z = 4$) and the trilayer has 132 atoms ($Z = 6$). Table 1 gives the structural and energy results for the bulk and optimized slabs.

Given the ionic nature of the hydroxylapatite mineral, surface relaxation/reconstruction processes are expected, due to the difference in the environment of the external ions compared with the same ions in the bulk structure. In fact, in the OHAp (001) ML structure model the surface relaxation is dramatic and unrealistic because of the small thickness, while in the thicker models only the upper and lower PO_4^{3-} planes, both about 3.4 Å from the surface, are relaxed. The internal layers in the BL and TL (001) OHAp structure are very close to the hydroxylapatite bulk geometry. The bi- and trilayer structures are also very similar, with only one more 'bulk' layer in the latter. Regarding the (010) surface of hydroxylapatite, surface relaxation phenomena are lower than those observed for the (001) slabs. From now on, we focus our discussion on the trilayer structures, because they are involved in the carbonated hydroxylapatite simulations presented below. In addition, to our knowledge, three-layered OHAp (001) and (010) surfaces have never been analysed at this QM level of theory.

In the (001) OHAp surface model (Fig. 2) it is possible to observe the inward displacement of the external calcium ions (Ca1 type) along the z axis by about 0.18 Å for each crystal face, with respect to its bulk position. The same effect occurs for the hydroxyl groups, with a mean displacement of 0.5 Å inward. At the same time, the external phosphate groups present their central atom with slightly changed x and y coordinates and an outward displacment along the z direction of 0.35 Å. These PO_4^{3-} tetrahedra also experience mean rotations of about 20° in the different spatial directions. According to these results, it is immediately clear that the

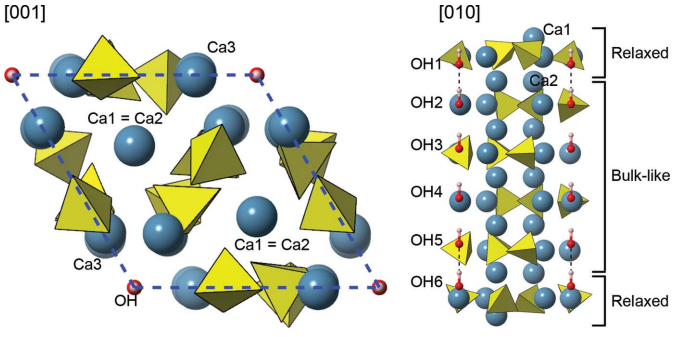

Figure 2
Views from the [001] (left) and [010] (right) directions of the optimized (001) OHAp trilayer surface. Symmetry equivalent Ca atoms are labelled Ca1, Ca2 and Ca3. Colour coding for atoms: cyan denotes calcium, yellow phosphor, red oxygen and pale pink hydrogen.

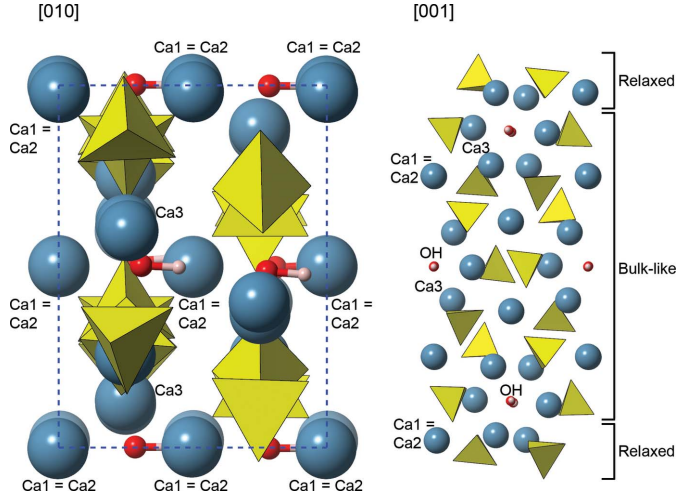

Figure 3
Views from the [010] (left) and [001] (right) directions of the optimized (010) OHAp trilayer surface. Symmetry equivalent Ca atoms are labelled Ca1, Ca2 and Ca3. Colour coding for atoms: cyan denotes calcium, yellow phosphor, red oxygen and pale pink hydrogen.

most accessible calcium ions are Ca1, followed by Ca3. Owing to their position, the Ca2 ions are not easily accessible because they are 3.1 Å deep in the structure.

Table 1 shows some selected mean bonds or interaction lengths from the surface structures, compared with the same distances observed in the OHAp bulk, from both theoretical (Ulian *et al.*, 2013*a*) and experimental results (Hughes *et al.*, 1989). All the mean values were calculated using all the bonds/interactions that are present in the structures. From the comparison with the hydroxylapatite bulk, in the (001) surface structures the mean P O bond length is slightly increased, whereas the mean Ca O electrostatic interaction shrinks. Despite the minimal variation in the O H bond length (0.001 Å, only in the TL), the relaxation of the (001) surface has brought the external OH groups (in both the top and bottom layers) nearer to the next ones in the column. This displacement leads to the formation of two hydrogen bonds at a mean distance of 1.99 Å. In the bulk structure, the OH OH distance is 2.48 Å, too high to allow hydrogen-bond formation. From Fig. 1, the TL structure exhibits OH1 OH2 and OH5 OH6 distances of 1.89 and 2.08 Å, respectively. Compared with the bulk, the pairs OH2/OH3 and OH4/OH5 are also nearer (2.24 and 2.34 Å, respectively), whereas the OH3 OH4 distance is increased to 2.59 Å.

In the (010) slab model (Fig. 3) it is possible to note at the external surface an inward displacement of the Ca1 and Ca3 ions by about 0.3 Å and an outward movement of the Ca3 ions by about 0.2 Å, with the overall result of the external calcium ions almost lying on a plane. Furthermore, the Ca3 displacements deform the hexagonal calcium channel. Phosphate groups at the surface are tilted by about 5°. As also observed for the (001) OHAp surface model, the mean P O bond distance is slightly greater than that of bulk hydroxylapatite, whereas the Ca O electrostatic interactions are shorter. The surface OH OH interaction distance within the same slab cell is 2.28 Å, which is smaller than that in bulk OHAp (2.48 Å), but it was observed that the interaction distance between hydroxyl groups belonging to neighbouring slab cells is increased to 2.73 Å. However, in the bulk-like layers the OH OH distances, both within and outside the slab cell, are about 2.49 Å, very close to those from the bulk.

The overall observed relaxation effects on the (001) and (010) hydroxylapatite models are related to the necessity to compensate for the ionic charges, positive and negative, of the different ions at the surface layers.

The surface formation energy ($E_{\rm surf}$) was computed as

$$E_{\rm surf} = \frac{E_{\rm slab} - NE_{\rm bulk}}{2A}, \qquad (1)$$

in which $E_{\rm slab}$ is the energy of the slab unit cell, N is the number of bulk unit cells with energy $E_{\rm bulk}$ and A is the surface unit-cell area. Since the models contain two surfaces, one at the top and one at the bottom, it is necessary to take into account the factor 2 in the formula. Also, in the case of the (001) OHAp surface, this expression gives the mean surface energy between two not completely equivalent faces, as one exposes a hydrogen atom and the other an oxygen atom.

The surface formation energies of both the (001) and (010) OHAp surfaces reach convergence with bilayer slabs, with values of 1.147 and 1.412 J m^{-2}, respectively. The calculated (010) surface formation energy is higher than that of the TL (001) layer, because the number and type of bonds that must be cut to define the (010) surface impart a higher formation energy compared with the (001) surface. Thus, the (010) OHAp surface is expected to be more active toward adsorption than the (001) one. These observations support and confirm the previous results of Corno *et al.* (2009, 2007) obtained with pseudopotentials on Ca atoms. However, we observed small differences between our surface formation energies and those obtained by Corno and co-workers, where the (001) $E_{\rm surf}$ = 1.043 J m^{-2} and the (010) $E_{\rm surf}$ = 1.709 J m^{-2}. The (001) monolayer structure needs less energy than the others for its formation, whereas the bi- and trilayers of OHAp have very similar $E_{\rm surf}$. This could be due to the different basis set employed, *i.e.* pseudopotentials on Ca ions in the work of Corno and co-workers and the adoption of an all-electron basis set in the present paper. Other values of (001) $E_{\rm surf}$ and (010) $E_{\rm surf}$ are reported in literature, which are related to both the initial surface model and the QM approach. For example, Rulis *et al.* (2007) obtained OHAp (001) $E_{\rm surf}$ = 0.871 J m^{-2} using the *VASP* and *OLCAO* codes (plane wave basis set), a Perdew Burke Ernzerhof (PBE) Hamiltonian and an $E_{\rm cutoff}$ of 600 eV. Filgueiras *et al.* (2006) employed the *METADISE* code (interatomic potential model) to run energy minimizations of two hydroxylapatite (001) surfaces with two different terminations. The first termination was PO_4 Ca PO_4 PO_4 Ca Ca and the second one was Ca Ca. The authors obtained surface formation energies of 1.08 and 1.12 J m^{-2}, respectively. Regarding the hydroxylapatite (010) surface, Astala & Stott (2008) calculated $E_{\rm surf}$ = 1.20 1.68 J m^{-2} with the *SIESTA* code (GTF-based) and a PBE functional.

The increasing trend in the (001) surface formation energy suggests an instability of the whole structure that can be related to the ferroelectric alignment of the OH group in the structure, according to previous studies (Corno *et al.*, 2007, 2010). This feature leads to the instauration of a dipole moment (see below) that increases proportionally with slab thickness. In the work of Corno *et al.* (2007), the simulation by a molecular mechanics approach of slab models from mono- to nonalayer showed that the band gap of OHAp decreases with structure thickness, resulting in a possible collapse of the whole structure at about 100 Å thick (a 15-layer structure). We conducted a test with the QM/DFT method used for the other three models on the electronic energy convergence of a tetralayered (thickness of about 27 Å) OHAp structure. This resulted in an instability in the electronic structure due to a possible conductive state, which is impossible for an ionic mineral. However, it is known that, in nature, the hydroxylapatite mineral is commonly found in rocks as a monoclinic structure (space group $P2_1/b$) that presents an antiferroelectric organization of the OH groups. Also, the monoclinic to hexagonal transition occurs at a relatively high temperature (Suetsugu *et al.*, 1998), which means that it needs a lot of

Table 2

Comparison between lattice vector, surface area A, mean bond lengths (Å) and surface formation energy E_{surf} of the trilayer (TL) structure of the OHAp (001) and COHAp (001) surface models.

Standard deviations are reported in parentheses.

	a (Å)	b (Å)	A (Å^2)	⟨P O⟩ (Å)	⟨O H⟩ (Å)	⟨Ca O⟩ (Å)	⟨C O⟩ (Å)	E_{surf} (J m ^{2})
OHAp TL	9.330 (3)	9.330 (3)	75.393 (4)	1.554 (12)	0.972 (4)	2.42 (8)		1.147
001-*A*-Na2	9.330 (3)	9.279 (3)	75.200 (4)	1.546 (35)	0.969 (1)	2.38 (19)	1.294 (9)	0.976
001-*A*-Na6	9.335 (3)	9.287 (3)	75.225 (4)	1.553 (15)	0.967 (2)	2.43 (11)	1.295 (8)	1.019
001-*B*-Na2	9.414 (3)	9.395 (3)	76.272 (4)	1.554 (13)	0.970 (1)	2.33 (10)	1.291 (11)	0.873
001-*B*-Na6	9.401 (3)	9.402 (3)	76.053 (4)	1.553 (13)	0.970 (1)	2.34 (11)	1.293 (9)	1.093
001-*AB*-Na2	9.364 (3)	9.347 (3)	75.776 (4)	1.553 (13)	0.968 (2)	2.42 (10)	1.294 (10)	0.906

energy to obtain a ferroelectric alignment of the OH groups. In recent simulations (Ulian *et al.*, 2013*a*), the symmetry of the OHAp bulk was reduced from $P6_3/m$ to $P6_3$ because of the non-physical replication of the hydroxyl groups in the calcium channel. In the models presented in this paper, the same approach was maintained. Probably, with increasing thickness of the slab, the system would prefer hydrogen-disordered OH columns. With our QM modelling, the maximum OHAp slab thickness that can be simulated can not exceed 20 Å (a trilayer structure).

3.2. Carbonated hydroxylapatite (COHAp) (001) surface models

Starting from the initial model of the trilayer structure of OHAp presented above, it is possible to consider the inclusion of carbonate ions in several ways. In the present work, both type *A* and type *B* substitutions were considered. The type *A* carbonate defect involves the replacement of two hydroxyl groups, according to the reaction

$$[2OH^-]_{cell} + CO_3{}^{2-} \rightarrow [CO_3{}^{2-}]_{cell} + 2OH^-,$$

while type *B* carbonate ions enter the OHAp structure by replacing phosphate groups as

$$[PO_4{}^{3-}]_{cell} + [Ca^{2+}]_{cell} + CO_3{}^{2-} + Na^+ \rightarrow [CO_3{}^{2-}]_{cell} + [Na^+]_{cell} + PO_4{}^{3-} + Ca^{2+}.$$

The type *B* reaction presented above includes a charge-compensation mechanism based on Na^+/Ca^{2+} substitution. Both the position and orientation of the different substitutes were considered from previous work. Regarding type *A* carbonate ion substitution, several studies depicted the 'closed' configuration, namely a $CO_3{}^{2-}$ ion with one C O bond perpendicular to the *c*-axis direction, as the most stable one (Astala & Stott, 2005; Fleet & Liu, 2003; Ulian *et al.*, 2013*a*,*b*). For type B substitution, the carbonate ion occupies one of the triangular faces of the exiting $PO_4{}^{3-}$ ion and the sodium atoms prefer to occupy two positions near the defect, one in the hexagonal calcium channel and one outside the channel (Astala & Stott, 2005; Fleet & Liu, 2007, 2004; Ulian *et al.*, 2014).

The modelling of COHAp (001) surfaces must take into account the position of both the carbonate defect (at the mineral/vacuum interface or in the bulk-like layer) and the charge-compensating ion (Na^+). Given the interest in surface charge and electrostatic potential modifications related to carbonate ion substitutions, in the present work the modelling involved the trilayer OHAp model previously described, where the type *A* and type *B* defects were introduced simultaneously. Five different COHAp (001) surface models were considered:

(i) A type *A* carbonate ion exposed on the surface and a type *B* one in the bulk-like layer, with the sodium ion occupying a Ca2 site (model labelled 001-*A*-Na2).

(ii) A type *A* carbonate ion exposed on the surface and a type *B* one in the bulk-like layer, with the sodium ion occupying a Ca3 site (model labelled 001-*A*-Na6).

(iii) A type *B* carbonate ion exposed on the surface and a type *A* one in the bulk-like layer, with the sodium ion occupying a Ca2 site (model labelled 001-*B*-Na2).

(iv) A type *B* carbonate ion exposed on the surface and a type *A* one in the bulk-like layer, with the sodium ion occupying a Ca3 site (model labelled 001-*B*-Na6).

(v) Both type *A* and type *B* carbonate ions exposed on the surface, with the sodium ion occupying a Ca2 site (model labelled 001-*AB*-Na2).

According to the experimental X-ray diffraction refinement of Fleet & Liu (2003), the type *A* carbonate ion in bulk apatite belongs to the $P\overline{3}$ space group, with six equivalent orientations in the calcium channels related to the threefold rotation axis and the inversion centre. However, in this work we initially placed the type *A* $CO_3{}^{2-}$ ion with the same orientation as was found in our previous work (Ulian *et al.*, 2013*b*), because recently it was demonstrated that the starting orientation in the Ca^{2+} channel does not compromise the final simulation result, as the carbonate ion has a very small rotational barrier (Peccati *et al.*, 2014).

The geometry optimizations were carried out without any symmetry constraints (space group *P*1), because the introduction of carbonate defects removes all symmetric features of the pure OHAp slab (space group *P*3). Furthermore, the absence of symmetry allows freedom in the geometric rearrangement of the slab's internal structure and parameters. Structural and energy results are reported in Table 2.

The results show that the presence of carbonate ion substitutions has a negligible influence on the surface relaxation processes, as can be observed in Fig. 4. Both type *A* and type *B* carbonate ions in the apatite environment maintain their typical bulk configurations. It is worth noting that, during geometric optimization of the 001-*A*-Na2 and 001-*A*-Na6

models (type *A* carbonate ion exposed at the surface), the CO_3^{2-} ion is rotated by about 120° around an axis passing through the C atom and perpendicular to the molecular plane. When the rotation was about 60°, the *CRYSTAL14* software found a transition state, with the carbonate ion in an 'open' configuration (a C O bond parallel to the [001] direction). This effect is probably related to surface termination, which has modified the type *A* carbonate ion environment and then affected the carbonate ion rotational barriers.

The surface formation energy of the different COHAp models was computed with this formula:

$$E_{\rm surf} = \frac{E_{\rm slab} - \left(E_{\rm bCAp\text{-}A} + E_{\rm bCOHAp\text{-}B\text{-}NaX} + E_{\rm bOHAp}\right)}{2A}, \quad (2)$$

where $E_{\rm bCAp\text{-}A}$ and $E_{\rm bCOHAp\text{-}B\text{-}NaX}$ are the bulk energies of type *A* carbonated apatite (CAp) and of type *B* COHAp with Na ions replacing calcium in position *X* (2 or 6), respectively, and *A* is the surface area. These energy values were previously calculated using the same computational parameters as those adopted here (Ulian *et al.*, 2013*a*, 2014). The $E_{\rm surf}$ term indicates that obtaining a (001) surface of COHAp, with the carbonate defect in an external layer, is energetically favoured. This result suggests that the CO_3^{2-} ion interrupts the ferroelectric effect produced by the OH alignment and consequently provides stability to the whole structure. Furthermore, the COHAp surface energy is lower than that of stoichiometric hydroxylapatite, which means that the carbonated (001) surface is less reactive and more stable than the pure one. The presence of carbonate ions reduces the OHAp internal order and entropically stabilizes the structure, in accordance with previous observations (Suda *et al.*, 1995).

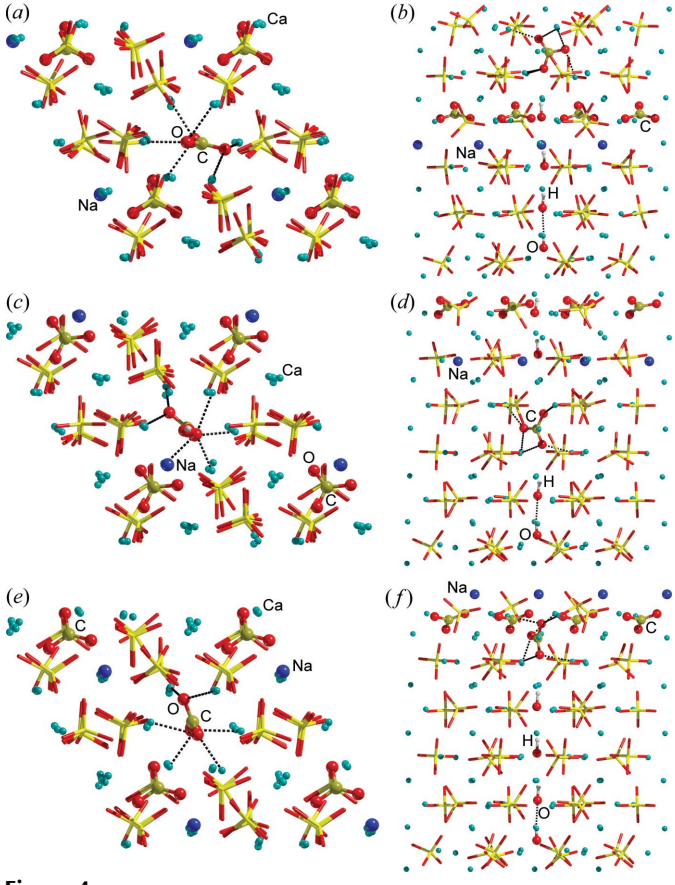

Figure 4
Views from the [001] (left) and [010] (right) directions of the optimized (001) surface of the (*a*), (*b*) 001 *A* Na2, (*c*), (*d*) 001 *B* Na6 and (*e*), (*f*) 001 *AB* Na2 models. Phosphate groups are represented as sticks and Ca atoms as small spheres for the sake of clarity. Colour coding for atoms: pale cyan denotes calcium, yellow phosphor, red oxygen, grey hydrogen, ochre carbon and blue sodium.

3.3. Carbonated hydroxylapatite (COHAp) (010) surface models

The procedure for including type *A* and type *B* carbonate ions in the (001) OHAp surface was also employed to model the COHAp (010) surface. The nomenclature adopted was the same as that used to identify the six (001) surface models, changing the prefix 001 to 010. Geometric results are reported in Table 3.

As observed for the (001) surfaces, the presence of carbonate ion substitutions does not have an influence on the surface relaxation processes, and both type *A* and type *B* carbonate ions in the apatite environment maintain their typical bulk configuration. Graphical representations of the 010-*A*-Na2, 010-*B*-Na2 and 010-*AB*-Na2 models are reported in Fig. 5. Note that a type *A* carbonate ion exposed on the surface always directs the C O bond perpendicular to the calcium channel ion direction towards the vacuum region (see Figs. 5*b* and 5*f*) because of the surface termination.

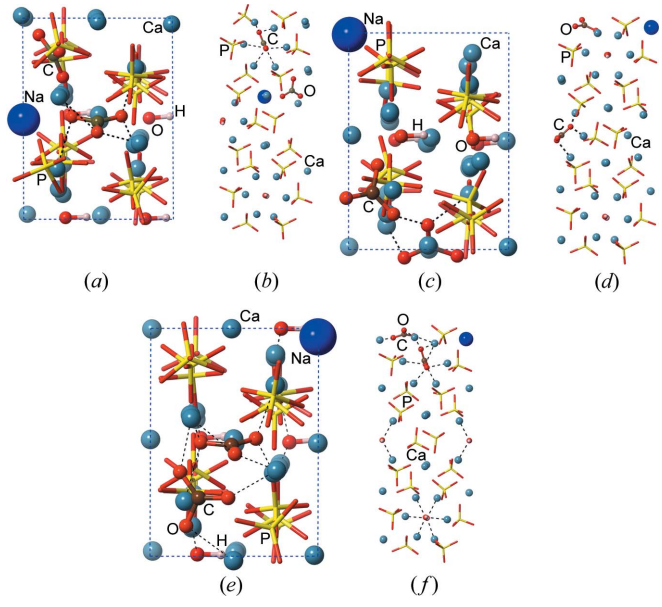

Figure 5
Views from the [010] (left of each pair) and [001] (right of each pair) directions of the optimized (010) surface of the (*a*), (*b*) 010 *A* Na2, (*c*), (*d*) 010 *B* Na6 and (*e*) and (*f*) 010 *AB* Na2 models. Phosphate groups are represented as sticks and Ca atoms as small spheres for the sake of clarity. Colour coding for atoms: cyan denotes calcium, yellow phosphor, red oxygen, pale pink hydrogen, dark brown carbon and blue sodium.

Table 3
Comparison between lattice vector, surface area A, mean bond lengths and surface formation energy E_{surf} of the trilayer (TL) structure of the OHAp (010) and COHAp (010) surface models.

Standard deviations are reported in parentheses.

	a (Å)	b (Å)	A (Å^2)	⟨P O⟩ (Å)	⟨O H⟩ (Å)	⟨Ca O⟩ (Å)	⟨C O⟩ (Å)	E_{surf} (J m ^{2})
OHAp TL	9.351 (3)	6.927 (2)	64.773 (4)	1.553 (22)	0.971 (1)	2.48 (8)		1.432
010-*A*-Na2	9.330 (3)	6.935 (2)	64.705 (4)	1.555 (23)	0.971 (1)	2.42 (9)	1.294 (14)	1.225
010-*A*-Na6	9.328 (3)	6.880 (2)	64.174 (4)	1.554 (17)	0.971 (2)	2.39 (27)	1.295 (20)	1.206
010-*B*-Na2	9.340 (3)	6.910 (2)	64.532 (4)	1.553 (19)	0.971 (1)	2.42 (10)	1.294 (20)	1.121
010-*B*-Na6	9.366 (3)	6.921 (2)	64.824 (4)	1.554 (20)	0.971 (9)	2.42 (10)	1.293 (14)	1.146
010-*AB*-Na2	9.352 (3)	6.884 (2)	64.380 (4)	1.553 (18)	0.971 (1)	2.38 (10)	1.296 (18)	1.188

We calculated the surface formation energies as we did previously for the (001) COHAp surfaces and these are reported in Table 3. Again, the results show that it is easier to cut an (010) carbonated hydroxylapatite than a stoichiometric OHAp one because of the entropy stabilization discussed previously. However, the different (010) COHAp surfaces are more energetic (and thus more reactive) than the (001) surfaces (see Table 2), following the trend observed for stoichiometric (001) and (010) OHAp.

3.4. Electrostatic potential of (carbonated) hydroxylapatite (001) surfaces

Both the pure and the defective OHAp have a strong ionic character, and knowledge of their surface potential features is an important predictive tool in understanding adsorption processes in close proximity to the (001) surface.

Electrostatic potential maps, mapped on an electron-density surface of constant value (10^{-4} a.u.) on the (001) OHAp TL and (001) COHAp surface model structures, are shown in Fig. 6. In general, the dominant electrostatic properties are given by the calcium and phosphate groups.

The hydroxylapatite surface (Fig. 6*a*) exhibits triangular regions of positive potential centred on the Ca1 sites and with three Ca3 ions in the vertexes. The red regions are related to negative potentials due to the PO_4^{3-} groups and present central small holes of neutrality at the Ca2 site. At the OH site, a slightly positive potential is reported in the top map and a very weak negative potential is present in the bottom map (not shown in Fig. 6). This effect is due to the atom in the OH that is exposed to the surface, H in the top layer and O in the bottom one, and represents a confirmation of the dipole moment generated by the ferroelectric alignment of the hydroxyl groups. This result is in excellent agreement with previous investigations by Corno and co-workers for their bilayer model (Corno *et al.*, 2010).

The type *A* $CO_3^{2-}/2OH^-$ substitution at the surface causes a distortion of the triangular positive and negative potential regions in the top layer (Figs. 6*b* and 6*c*). The centre of the calcium channel has a weak positive potential, because the carbonate ion is half-way down in the six-calcium ring and the small positive potential due to the hydroxyl group is lost. The charge-balancing sodium ion, related to type *B* defects in the bulk-like layer, has a strong neutralizing effect when it occupies one of the six calcium-channel positions, whereas no visible effects were noticed in the other case. When type *B* carbonate substitution is exposed at the surface, the electrostatic potential completely loses its triangular pattern in favour of alternating 'stripes' of positive and negative potentials (Figs. 6*d* and 6*e*). The sodium ion, in this case, confines the positive region slightly because of its smaller positive valence than calcium. The combination of type *A* and *B* defects exposed at the surface (Fig. 6*f*) partially restores the surface triangular pattern, increasing the areas of negative potential. The observed modulations of the electrostatic features are striking, varying according to the carbonate ion position in the slab models, and they open new possibilities for understanding the interaction of carbonated hydroxylapatite with the biological environment.

To investigate further the potential modulation induced by the carbonate defect in the calcium channel, electrostatic potential sections (maps), made in a plane perpendicular to

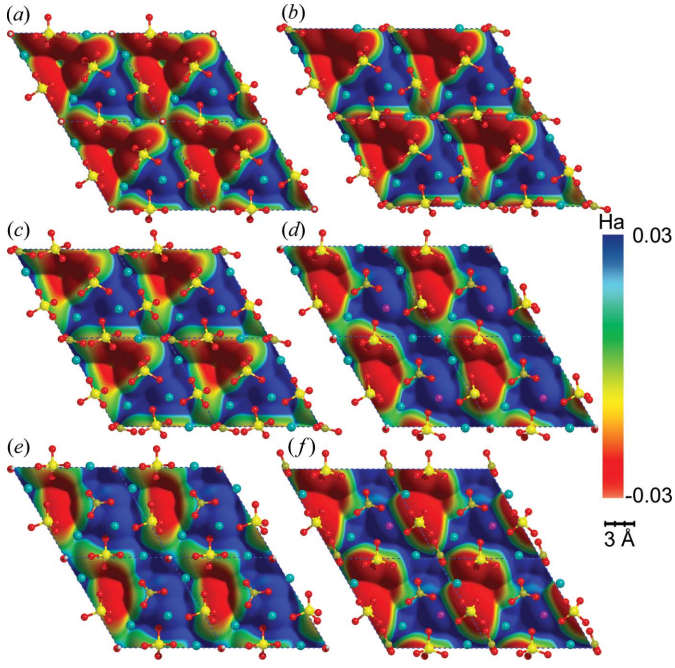

Figure 6
Top views along the [001] direction of the (001) surfaces of TL models: (*a*) stoichiometric OHAp, (*b*) 001 *A* Na2, (*c*) 001 *A* Na6, (*d*) 001 *B* Na2, (*e*) 001 *B* Na6 and (*f*) 001 *AB* Na2. The three dimensional electrostatic potential is mapped onto a surface of constant electron density (10^{-4} a.u.) from 0.03 to 0.03 a.u. For the sake of clarity, four unit cells were considered for each map.

the [100] direction that contains the OH groups, were considered and these are reported in Fig. 7. It is possible to distinguish in contour maps of both OHAp and carbonated hydroxylapatite alternating positive areas on the calcium ions and negative areas on the phosphate groups. The type *A* carbonate ion plays a fundamental role in interrupting the dipole moment generated by the OH ferroelectric alignment (grey arrow in Fig. 7*a*). In hydroxylapatite there are small zones of negative potential corresponding to the phosphate groups. The presence of substitutional defects causes a wide variation, with strong positive areas on the upper surface (due to Ca1 ions) and a negative potential on the opposite one. Furthermore, it is possible to observe that the CO_3^{2-} ion at the surface, in either the type *A* or type *B* model, seems to enhance the positive potential regions relating to Ca1 ions.

Finally, the electrostatic potential was computed on a two-dimensional grid of points parallel to the (001) surface and placed at 2 Å from the topmost Ca ion, for both OHAp and COHAp structures. The results are presented in Fig. 8 as rendered two-dimensional contour level maps that show the positive poles of electrostatic potential associated with the Ca ions and the negative regions due to the surface phosphate groups. The immediately visible effect due to external type *A* carbonate substitution is the distortion of the isopotential lines, especially in the PO_4^{3-} negative region (Figs. 8*b* and 8*c*). When the surface CO_3^{2-} ion is from type *B* substitution, it is possible to observe a modification of the positive region into stripe-like structures and a reduction in the negative potential of the phosphate groups (Figs. 8*d* and 8*e*). The co-presence at the surface of both type *A* and type *B* carbonate ions (Fig. 8*f*) results in a potential map with both positive and negative stripe-like regions about 5 Å wide. The two-dimensional maps obtained for the OHAp TL slab (Fig. 7*a* and 8*a*) are in good agreement with the previous results of Corno *et al.* (2007).

3.5. Electrostatic potential of (carbonated) hydroxylapatite (010) surfaces

The three-dimensional electrostatic potential maps and the two-dimensional maps at 2 Å from the surface were also computed for both OHAp and COHAp (010) surface models, reported in Figs. 9 and 10, respectively.

The pure hydroxylapatite potential maps (Figs. 9*a* and 10*a*) show interconnected stripes (*ca* 5 Å wide) of strongly positive potential (blue colour) alternating with corresponding ones of negative value (red colour), in good agreement with previous results (Corno *et al.*, 2010). It is thus expected that the local

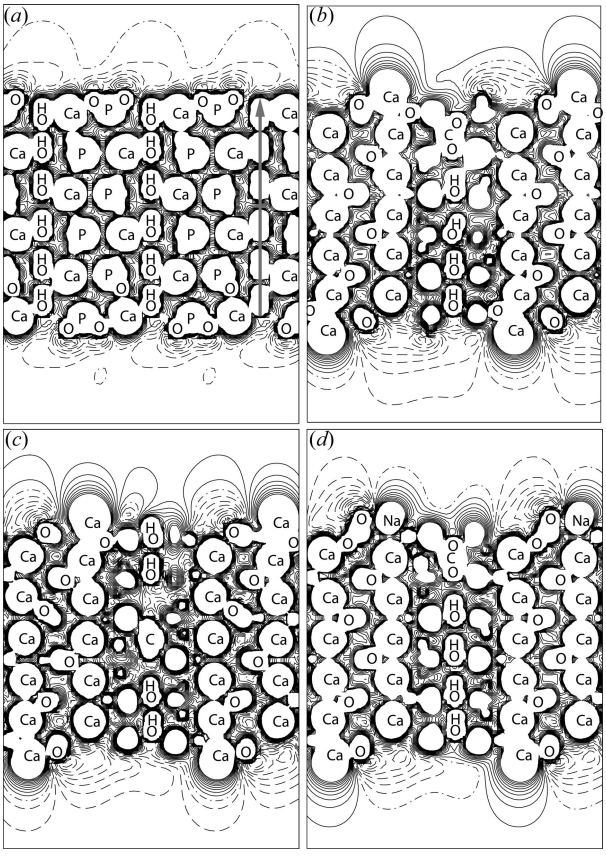

Figure 7
Electrostatic potential contour maps of trilayer slab models: (*a*) OHAp (001), (*b*) 001 *A* Na6, (*c*) 001 *B* Na6 and (*d*) 001 *AB* Na2. The sections are made on the planes containing OH and OH/C(CO_3^{2}), respectively. Continuous lines represent positive values and dashed lines negative values, while dash dotted lines indicate the zero level. Isolines are separated by 0.01 a.u.

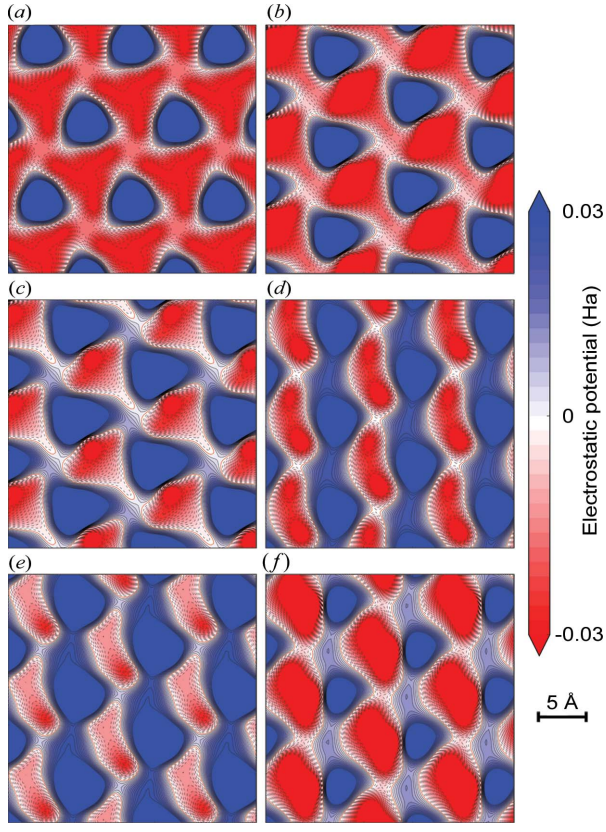

Figure 8
Electrostatic potential contour maps obtained from a plane perpendicular to the [001] direction and placed at 2 Å from the topmost calcium ion of the (*a*) OHAp, (*b*) 010 *A* Na2, (*c*) 010 *A* Na6, (*d*) 010 *B* Na2, (*e*) 010 *B* Na6 and (*f*) 010 *AB* Na2 models. Continuous lines represent positive values and dashed lines negative values, while dash dotted lines are the zero level. Isolines are separated by 0.002 hartree.

polarity at the (010) surface exerts a powerful action on dipolar molecules like water or amino acids. As reported in the *Introduction*, this face is rather extended in the OHAp morphology (Fig. 1), so it plays a very relevant role in adsorption. Indeed, the (010) face is expected to modulate the interaction of the collagen rod with proline and hydroxylproline, owing to the alignment of the *c* axis of OHAp platelets with the protein (Dorozhkin, 2009; Dubey & Tomar, 2009).

The presence of a type *A* carbonate ion on the surface seems to alter both the direction of the stripes (canted by about 45°) and the intensity of the potential. In contrast with what was observed in the present study for the 001-*A*-Na models (Figs. 6*b* and 6*c*), in the corresponding (010) surfaces there is an increase of the positive region at the expense of the negative one (Figs. 9*b* and 9*c*). When a type *B* defect is exposed on the surface, we note that the positive regions are much larger than the negative regions, and the stripe-like pattern is almost lost. Islands of weak negative potential are located in positions corresponding to phosphate groups, and type *B* carbonate ions provide a small extension to these negative regions. In model 010-*B*-Na6 there is even a positive potential surrounding the carbonate ion. In each case, the opposite surfaces of the carbonate-substituted models display an electrostatic potential pattern very close to that of stoichiometric hydroxylapatite, which means that the surface property variations are only affected at a small distance from the substitutions. This may explain the weak contribution of type *A* CO_3^{2-} to the potential modulation, as the substituting ion is located a few ångströms below the surface, whereas type *B* substitutions, which are directly exposed to the vacuum region, greatly affect this property. This is also reflected in the 010-*AB*-Na2 model, with potential features mainly dominated by type *B* carbonate ions and slightly affected by type *A* substitutions (Figs. 9*f* and 10*f*).

If we compare all the surface potentials of (carbonated) hydroxylapatite with each other, the main result is that (010) surfaces are more easily modulated in their electrostatic

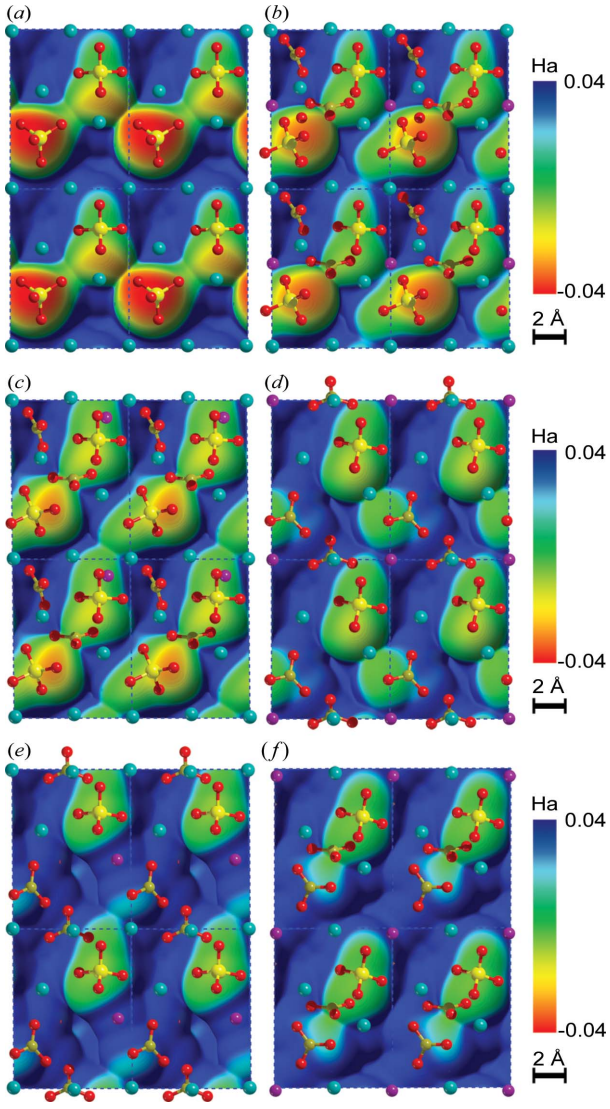

Figure 9
Top views along the [010] direction of the (010) TL surfaces of the (*a*) OHAp, (*b*) 010 *A* Na2, (*c*) 010 *A* Na6, (*d*) 010 *B* Na2, (*e*) 010 *B* Na6 and (*f*) 010 *AB* Na2 models. The three dimensional electrostatic potential is mapped onto a surface of constant electron density (10^{-4} a.u.) in the range ±0.03 a.u. For the sake of clarity, four unit cells were considered for each map.

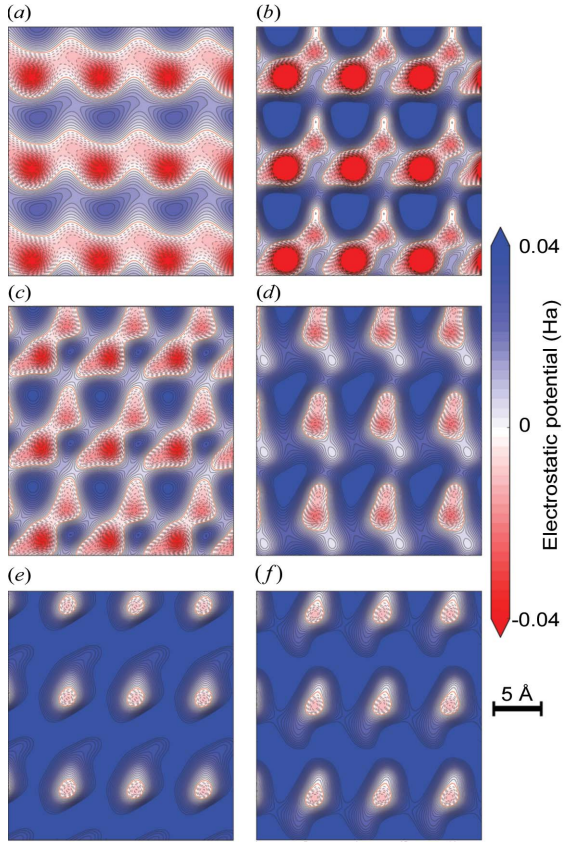

Figure 10
Electrostatic potential contour maps obtained from a plane perpendicular to the [010] direction and placed at 2 Å from the topmost calcium ion of the (*a*) OHAp, (*b*) 010 *A* Na2, (*c*) 010 *A* Na6, (*d*) 010 *B* Na2, (*e*) 010 *B* Na6 and (*f*) 010 *AB* Na2 models. Continuous lines represent positive values and dashed lines negative values, while dash dotted lines are the zero level. Isolines are separated by 0.002 hartree.

potential than (001) surfaces. A strong similarity can be observed in the potential map of Fig. 9(*a*) with those of Figs. 6(*d*) 6(*f*), as each map contains alternating positive and negative stripe-like regions of electrostatic potential. Remembering that the (010) hydroxylapatite surface is the one most involved with adsorption processes, this striking feature suggests that the carbonate ion substitutions may mimic on the (001) OHAp surface the electrostatic properties of the (010) one, and they could be related to important biomolecule interactions that need to be further investigated. However, this is beyond the scope of the present paper, which is focused on the structural and surface potential properties of carbonate-substituted apatites.

4. Conclusions

In this work we have presented *ab initio* simulations at the B3LYP level of theory on several (001) and (010) carbonated hydroxylapatite surface models. Three-layer models with carbonate ion substitutions in different positions (on the exposed surface and in the bulk-like layer) were analysed in their crystallographic and surface potential details. The results show that stoichiometric (010) hydroxylapatite slab models have a greater energy of surface formation than (001) ones, in good agreement with previous theoretical data reported in the literature. The presence of carbonate defects in the apatite structure reduces the energy needed to cut a surface because of entropy stabilization, while maintaining the trend $E_{\rm surf}(010) > E_{\rm surf}(001)$. However, carbonate ions do not affect surface relaxation processes significantly. The hydroxylapatite surface potential is strongly modulated by the presence of carbonate ions in a small thickness of the mineral.

Another relevant observation from this work is that the trilayer slab is an adequate model that can be employed to simulate the surface adsorption of relevant molecules like water, carbon monoxide and amino acids on carbonated hydroxylapatite. This is a current project under development in our laboratory.

The presented results could be helpful to researchers involved and interested in the investigation of apatite organic matter interactions in various and differing fields, such as biotechnology, biomedicine, analytical chemistry, and crystal synthesis and design.

Acknowledgements

The authors wish to thank the University of Bologna, Italy, for funding this research through the FARB Linea 2 project 2013 2015.

References

Astala, R. & Stott, M. J. (2005). *Chem. Mater.* **17**, 4125 4133.
Astala, R. & Stott, M. J. (2008). *Phys. Rev. B*, **78**, 075427.
Becke, A. D. (1993). *J. Chem. Phys.* **98**, 1372 1377.
Canepa, P., Chiatti, F., Corno, M., Sakhno, Y., Martra, G. & Ugliengo, P. (2011). *Phys. Chem. Chem. Phys.* **13**, 1099 1111.
Corno, M., Busco, C., Bolis, V., Tosoni, S. & Ugliengo, P. (2009). *Langmuir*, **25**, 2188 2198.
Corno, M., Orlando, R., Civalleri, B. & Ugliengo, P. (2007). *Eur. J. Mineral.* **19**, 757 767.
Corno, M., Rimola, A., Bolis, V. & Ugliengo, P. (2010). *Phys. Chem. Chem. Phys.* **12**, 6309 6329.
Coxon, F. P., Thompson, K. & Rogers, M. J. (2006). *Curr. Opin. Pharmacol.* **6**, 307 312.
Dangaria, S. J., Ito, Y., Yin, L. L., Valdrè, G., Luan, X. H. & Diekwisch, T. G. H. (2011). *Tissue Eng. A*, **17**, 279 290.
Dorozhkin, S. V. (2009). *Materials*, **2**, 399 498.
Dorozhkin, S. V. (2010*a*). *Acta Biomater.* **6**, 715 734.
Dorozhkin, S. V. (2010*b*). *Biomaterials*, **31**, 1465 1485.
Dovesi, R., Roetti, C., Freyria Fava, C., Prencipe, M. & Saunders, V. R. (1991). *Chem. Phys.* **156**, 11 19.
Dovesi, R., Saunders, V. R., Roetti, C., Orlando, R., Zicovich Wilson, C. M., Pascale, F., Civalleri, B., Doll, K., Harrison, N. M., Bush, I. J., Llunell, M., Causà, M. & Noel, Y. (2014). *CRYSTAL14 User's Manual.* University of Torino, Italy.
Dubey, D. K. & Tomar, V. (2009). *J. Mech. Phys. Solids*, **57**, 1702 1717.
Filgueiras, M. R. T., Mkhonto, D. & de Leeuw, N. H. (2006). *J. Cryst. Growth*, **294**, 60 68.
Fleet, M. E. (2009). *Biomaterials*, **30**, 1473 1481.
Fleet, M. E. & Liu, X. Y. (2003). *J. Solid State Chem.* **174**, 412 417.
Fleet, M. E. & Liu, X. Y. (2004). *J. Solid State Chem.* **177**, 3174 3182.
Fleet, M. E. & Liu, X. (2007). *Biomaterials*, **28**, 916 926.
Hay, P. J. & Wadt, W. R. (1985). *J. Chem. Phys.* **82**, 284 298.
Hughes, J. M., Cameron, M. & Crowley, K. D. (1989). *Am. Mineral.* **74**, 870 876.
Kirkham, J., Brookes, S. J., Shore, R. C., Wood, S. R., Smith, D. A., Zhang, J., Chen, H. F. & Robinson, C. (2002). *Curr. Opin. Colloid Interface Sci.* **7**, 124 132.
Lee, C. T., Yang, W. T. & Parr, R. G. (1988). *Phys. Rev. B*, **37**, 785 789.
Leu, C. T., Luegmayr, E., Freedman, L. P., Rodan, G. A. & Reszka, A. A. (2006). *Bone*, **38**, 628 636.
Ma, G. B. & Liu, X. Y. (2009). *Cryst. Growth Des.* **9**, 2991 2994.
Mkhonto, D. & de Leeuw, N. H. (2002). *J. Mater. Chem.* **12**, 2633 2642.
Momma, K. & Izumi, F. (2008). *J. Appl. Cryst.* **41**, 653 658.
Nancollas, G. H., Tang, R., Phipps, R. J., Henneman, Z., Gulde, S., Wu, W., Mangood, A., Russell, R. G. G. & Ebetino, F. H. (2006). *Bone*, **38**, 617 627.
Pascale, F., Zicovich Wilson, C. M., López Gejo, F., Civalleri, B., Orlando, R. & Dovesi, R. (2004). *J. Comput. Chem.* **25**, 888 897.
Peccati, F., Corno, M., Delle Piane, M., Ulian, G., Ugliengo, P. & Valdrè, G. (2014). *J. Phys. Chem. C*, **118**, 1364 1369.
Pezzotti, G., Rondinella, A., Marin, E., Zhu, W., Nicoli Aldini, N., Ulian, G. & Valdrè, G. (2016). *J. Mech. Behav. Biomed. Mater.* **65**, 264 273.
Prencipe, M., Pascale, F., Zicovich Wilson, C. M., Saunders, V. R., Orlando, R. & Dovesi, R. (2004). *Phys. Chem. Miner.* **31**, 559 564.
Rulis, P., Yao, H. Z., Ouyang, L. Z. & Ching, W. Y. (2007). *Phys. Rev. B*, **76**, 245410.
Simmer, J. P. & Fincham, A. G. (1995). *Crit. Rev. Oral Biol. Med.* **6**, 84 108.
Suda, H., Yashima, M., Kakihana, M. & Yoshimura, M. (1995). *J. Phys. Chem.* **99**, 6752 6754.
Suetsugu, Y., Shimoya, I. & Tanaka, J. (1998). *J. Am. Ceram. Soc.* **81**, 746 748.
Ugliengo, P., Viterbo, D. & Chiari, G. (1993). *Z. Kristallogr.* **207**, 9 23.
Ulian, G., Valdrè, G., Corno, M. & Ugliengo, P. (2013*a*). *Am. Mineral.* **98**, 410 416.
Ulian, G., Valdrè, G., Corno, M. & Ugliengo, P. (2013*b*). *Am. Mineral.* **98**, 752 759.
Ulian, G., Valdrè, G., Corno, M. & Ugliengo, P. (2014). *Am. Mineral.* **99**, 117 127.
Vallet Regì, M. & Gonzàlez Calbet, J. M. (2004). *Prog. Solid State Chem.* **32**, 1 31.
Zhang, Y. H. *et al.* (2009). *J. Am. Chem. Soc.* **131**, 5153 5162.